Water permeability of sunlit lunar highlands regolith using LHS-1 simulant

Tabuchi, Yoshiki
Cooperative Program for Resources Engineering, Graduate School of Engineering, Kyushu University

Kioka, Arata
Cooperative Program for Resources Engineering, Graduate School of Engineering, Kyushu University

Yamada, Yasuhiro
Cooperative Program for Resources Engineering, Graduate School of Engineering, Kyushu University

https://hdl.handle.net/2324/6796420

出版情報：Acta Astronautica. 213, pp.344-354, 2023-12. Elsevier
バージョン：

Water permeability of sunlit lunar highlands regolith using LHS-1 simulant

Yoshiki Tabuchi (1), Arata Kioka (1,2,*), Yasuhiro Yamada (1,2)

1. Cooperative Program for Resources Engineering, Graduate School of Engineering, Kyushu University, Fukuoka 819-0395, Japan.
2. Department of Earth Resources Engineering, Faculty of Engineering, Kyushu University, Fukuoka 819-0395, Japan.

***Correspondence:**

A. Kioka: Department of Earth Resources Engineering, Faculty of Engineering, Kyushu University, Fukuoka 819-0395, Japan; +81-92-802-3343, kioka@mine.kyushu-u.ac.jp

Abstract

The regolith on the Earth's Moon has been attracting attention from the perspective of understanding the planetary surface processes and procuring in-situ resources. However, very few studies have investigated the hydraulic properties of the lunar regolith, which should pose one of the most significant physical properties for understanding the lunar surface processes and evaluating regolith utilizations. In this paper, we study the water permeability of the surficial regolith layer on sunlit lunar highlands using the lunar highlands regolith simulant LHS-1. We measure the water permeability of LHS-1 at packing fractions of 0.49–0.60 by simulating lunar gravitational environments and evaluating the influences of freeze-thaw, which is expected to occur on the sunlit lunar highland surfaces. Our results indicate that the water permeability of lunar highland regolith is one to two orders of magnitudes lower than that of fine silica sands and monodisperse spherical glass beads at the given packing fraction. The low water permeability of lunar highland regolith attributes to the regolith particles having irregular and angular shapes with sharp edges and micron-sized chunks due to the least weathering, unlike soil particles on the Earth. The horizontal water permeability of lunar highland regolith simulant before freeze-thaw is 1.6×10^{-13} m^2 at a packing fraction of 0.6. From the porosity-depth profile available from previous studies, we also obtained the water permeability-depth curve, representing the vertical water permeabilities of 6×10^{-13}–2×10^{-12} m^2 and 7×10^{-14}–3×10^{-13} m^2 at the lunar surface and the depth of 5 m within the surficial lunar regolith layer, respectively. We also found that the water permeability of lunar highland regolith increased after one freeze-thaw cycle, achieving 6.4 times higher than the permeability before the freeze, and the increase was more significant with lower packing fractions. We suggest that the pore water in the solid phase due to the freeze encourages the rearrangement of the regolith particles changing the total contact area between the particles. This study will help us better understand the abundance and distribution of molecular water on the lunar surface, lunar surface processes, and regolith utilizations.

Keywords

Freeze-thaw; Lunar regolith; Moon; Regolith simulant; Water permeability

Published in *Acta Astronautica*

Received 23 May 2023, Revised 14 September 2023, Accepted 18 September 2023.

https://doi.org/10.1016/j.actaastro.2023.09.027

Highlights

- Water permeability (WP) of lunar highland soils is estimated using simulant LHS-1
- WP before the freeze-thaw is 1.6×10^{-13} m^2 with a packing fraction (PF) of 60%
- WP-depth curve was estimated; e.g., WP can be 7×10^{-14}–3×10^{-13} m^2 at 5 m depth
- The change in WP before and after one freeze-thaw cycle was greater with lower PFs
- The tortuosity with a PF of 49% decreased by about 60% with the freeze-thaw

1. Introduction

The surfaces of the Earth's moon and Mars are covered by an unconsolidated and fragmented layer of debris known as the regolith [1]. The regolith on the Earth's moon and Mars has been attracting attention from the perspective of understanding the extraterrestrial surface processes and procuring in-situ resources. Also, a better understanding of regolith is vital for successful safe landings on the Moon and Mars. On the Earth's moon, the regolith is present throughout almost the entire lunar surface, accounting for approximately 4×10^5 km^3 of regolith on the entire lunar surface. An estimated average thickness of regolith on the lunar surface is expected to be ~10 m based on 70-cm wavelength Arecibo radar data, with generally hosting thicker regolith columns in the lunar highlands than the lunar lowlands and Mares [2,3,4]. Such thick regolith columns should play a profound role in various lunar surface processes, including the sediment and erosion dynamics, the water and gas exchanges at the regolith-overlying "atmosphere" interface, and possible life existence (e.g., [5]). The abundance of regolith has encouraged us to utilize it for the extraction of oxygen [6], cement materials [7], and plant growths aiming at stable food production [8] for the development of the lunar resources and establishing a base on the Moon.

The existence of water on the Moon has been of utmost interest in the recent decade. The presence of water in the lunar body has a considerable influence on the geological evolution of the body. Also, many studies found evidence of not only water ice in polar regions [9] but also molecular water in polar and even sunlit lunar surfaces (e.g., [10,11,12]). Although the surficial water abundance is likely very low, the water flow plays a crucial role in mass and heat transfer, water-regolith reactions, and possible subsurface microbial communities within the regolith column. The soil permeability within the regolith layer is among the most crucial parameters controlling fluid flow. Moreover, the regolith layer on the sunlit lunar highland surfaces is very likely exposed to freeze-thaw cycles, altering geotechnical properties and microstructure that should lead to a change in soil permeability as found on the Earth [13,14].

Soil permeability depends on the physical properties, porosity, and grain microstructure of soil. A few previous studies reported gas permeability of lunar and Martian soil and found that the gas permeability increases with lower porosity and larger particle size [15,16,17]. However, the gas permeability of terrestrial soil is several times to one order of magnitude larger than water permeability [18], suggesting that the water permeability of lunar regolith can be much lower than the reported gas permeability. To date, no studies to our best knowledge have reported water permeability of lunar regolith. Molecular water is unlikely enriched on the moon, yet its presence and abundance should relate to the water permeability of the lunar surface's sediment column. Also, understanding the permeability of the lunar regolith is essential to tailor appropriate strategies for future lunar explorations and utilizing the regolith to plant cultivations and concrete strength improvement for sustainable human habitability on the Moon [8,19,20,21]. Thus, the water permeability of lunar regolith is among the essential physical properties for a better understanding of the lunar surface processes and broad areas of the engineering and agricultural applications of regolith utilizations. Among the regolith layers in the upper crust, divided into the uppermost surficial regolith layer with a thickness of up to 20 m and the underlying Upper and Lower Megaregolith layers down to 20–25 km [22], the water permeability of the surficial regolith layer is most significant for investigating the lunar surface processes and the regolith utilization. In this study, we aim to estimate the water permeability of the surficial regolith layer in the lunar highlands using lunar highland regolith simulant LHS-1. We further investigate the influences of freeze-thaw on the water permeability of lunar highland regolith.

2. Materials and Methods

2.1. Studied materials and porous media samples

We used the Exolith Lab's high-fidelity Lunar Highlands Simulant LHS-1 (e.g., [8,23,24,25,26,27]) for measuring the water permeability of lunar regolith and its change due to freezing and thawing. The highland simulant LHS-1 is compositionally and physically similar to the actual highland regolith because LHS-1 is well characterized by lunar highlands regolith samples delivered by Apollo 16 [23,24]. We also measured water permeabilities of other granular materials, including fine silica sands K-6, K-7 (Kumamoto-Silica Mining Co., Ltd., Japan), T-7, T-8 (TOHOKU KEISYA Co., Ltd., Japan) and fine monodisperse nearly-spherical glass beads BZ-01 and BZ-02 (AS ONE Corporation, Japan), to compare with that of lunar highlands regolith. The physical properties of the studied granular materials are summarized in Table 1. Our Scanning Electron Microscope (SEM) imaging highlights that the surface microstructure of lunar highlands regolith simulant has an irregular and angular shape with sharp edges and micron-sized chunks (Figure 1). The silica sands and glass beds have a relatively smooth surface.

To measure the water permeability of the studied granular materials (see Section 2.2), we prepared the porous media column samples using 10-mm inner diameter and 200-mm long acryl pipes filled with the given studied granular material. To prevent water leakage, we reinforced the inlet and outlet of the given porous media sample using rubber plugs, nylon meshes, sealing tapes, and pressure-sensitive tapes, like the methods measured for glass beads and terrestrial soils in the previous studies [28,29]. The packing fraction of lunar highland regolith simulant within the porous media sample ranged from 49% to 60%, resulting in 40% to 51% porosity. The resulting porosities fall within the depths between ~0.1 m and ~5 m of the uppermost regolith column [30,31,32].

Table 1
Averaged grain density and median diameter of the studied granular materials.

Granular material	Grain density (g/cm^3)	Mean diameter (μm)
LHS-1	3.22	90
K-6	2.57	350
K-7	2.58	180
T-7	2.75	170
T-8	2.78	120
BZ-01	2.50	115
BZ-02	2.50	200

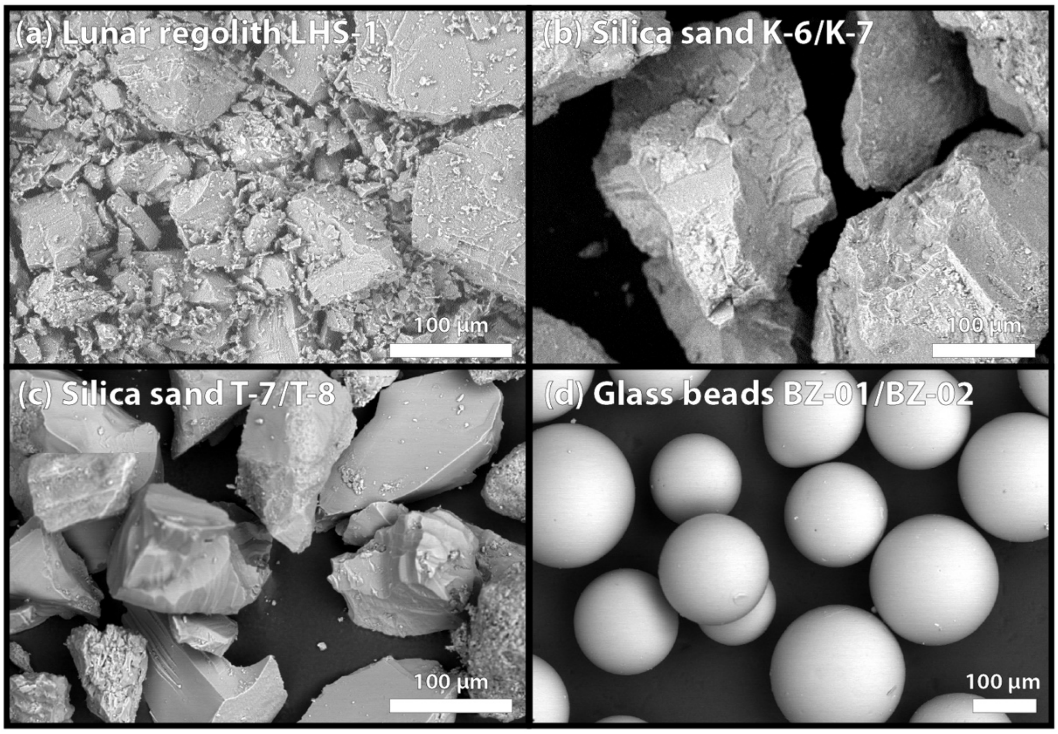

Figure 1
Scanning Electron Microscope (SEM) images of (a) lunar highlands regolith simulant LHS-1, (b) silica sand K-6, (c) silica sand T-8, and (d) glass beads BZ-02 used in this study. The SEM images were taken using JSM-IT700HR (JEOL, Ltd., Tokyo, Japan) at the Center of Advanced Instrumental Analysis, Kyushu University.

2.2. Water permeability measurement

Our water permeability measurement of the respective granular material (Table 1 and Figure 1) is similar to classic Darcy's experiment. The apparatus of our water permeability measurement includes plastic containers A and B, a water pump, a thermometer, a digital manometer, and the porous media sample column filled with the given studied granular materials (Figure 2). The clean tap water in plastic container A was pumped up to plastic container B which levels water at a certain height to control a slow water flow from plastic container B. The water is then fed into the porous media sample column [33]. The water flow is continuous and steady. The digital manometer measured the pressure difference between the outlet and inlet of the given sample column. When water (incompressible fluid) is used for permeability estimations, the permeability (intrinsic permeability) of the given sample k (m^2) was estimated by Darcy's law expressed by (e.g., [18]):

$$k = \frac{Q\mu L}{A\Delta p}, \quad (1)$$

where Q (m^3/s) is the volumetric flow rate, μ (Pa·s) is the dynamic viscosity of water, L (m) is the length of sample column (0.2 m), A (m^2) is the cross-sectional area of sample column (7.85×10^{-5} m^2), and Δp (Pa) is the pressure difference between outlet and inlet of the given sample column. The volumetric flow rate Q was measured over 3 min of water flowing out from the outlet of the given sample column. The dynamic viscosity of water μ, which depends on temperature, was calculated using the IAPWS Formulation 2008 [34]. Water temperature was constantly monitored with the thermometer equipped in the plastic container. The pressure difference Δp was continuously measured using the digital manometer FUSO-82153 (FUSO Co. Ltd., Japan). The pressure difference Δp fell within 2.92 – 10.08 kPa in our measurements, varying with the type of granular materials, packing fractions, simulated gravity fields, and the presence of freeze-thaw (see below). For the studied flow in porous media, the Reynolds number Re is defined by [35]:

$$Re = \frac{\rho_w Q \bar{D}}{A\mu(1-\phi)} = \frac{\rho_w Q \bar{D}}{A\mu\eta}, \quad (2)$$

where ρ_w is the density of water (kg/m^3), $\bar{D}$ is the mean diameter of granular bed (m), ϕ is the porosity of the porous media sample, and η is the packing fraction of the porous media sample. The Reynolds number in our permeability measurement ranged from 0.001 to 0.2 for all the tested granular materials. This indicated that the flow regime in our measurement was laminar, ensuring that Darcy's law was valid in our measurement [36]. The water permeability of the given granular material was calculated when the pressure difference Δp and the volumetric flow rate Q were kept constant. In reporting the measurement results, we present the measured values of water permeability as $\bar{k} \pm k_\sigma$ (m^2), where $\bar{k}$ and k_σ are the mean and one standard deviation of the multiple measurements of the given sample.

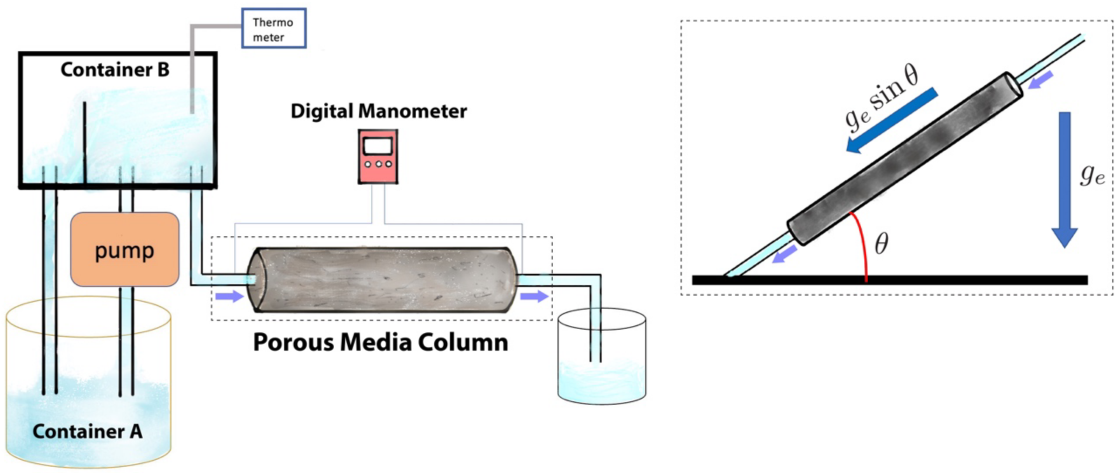

Figure 2
Apparatus of water permeability measurement. The angle θ represents the head-up tilt angle of the given sample to simulate the given gravity field g.

The water permeability of soil can be lower on the lunar surface than on Earth's surface due to the lower gravity. We thus further attempted to experimentally investigate the influence of lunar gravity on the water permeability of the tested granular materials, although only a few publications reported the geomechanical properties of extraterrestrial soil. The available methods simulating lunar gravity environments include the parabolic flight aircraft, drop tower, microgravity rocket, hydraulic gradient similitude method, and tilting method [37]. The parabolic flight aircraft and drop tower are limited to 0–30 s duration [38,39,40,41]. The microgravity rocket can provide a longer duration of up to 10 min, but it is relatively unstable and costly [42]. Therefore, we adopted the tilting method, in which the gravitational acceleration can be adjusted by controlling the weight and tilting angle of the sample [43,44]. The tilting method is the only method to produce very long-duration (longer than 10 min), continuous and steady water flow, and stable and controllable low gravitational fields, which are essential to the water permeability measurement. When the sample column was placed on the level, we simply measured the horizontal water permeability k_{xy} using Eq. (1), which can be zero-gravity "vertical" water permeability because gravity played no role in the water inlet-outlet direction [36]. On the other hand, we quantified the vertical water permeability $k_z(g)$ of the given gravity field g depending on the tilting angle of the sample column when it was not placed horizontally (Figure 2). We simulated several gravity fields g, including lunar gravity (0.17G), Martian gravity (0.38G), and Earth's gravity fields ($g_e = 1$G) by adjusting the head-up tilt angle (θ) of the given sample with 9.6±0.2°, 22.3±0.2°, and 90.0±0.2° using a digital inclinometer GLM 500 Professional (Robert Bosch GmbH, Germany). The tilting method is the only method currently available to measure the water permeability of the given gravity field other than the in-situ measurements on the lunar and Martian surfaces; however, our tilting method might generate additional undesirable stresses to the "actual" water flow by friction and lateral stresses on the water-regolith, water-pipe, and regolith-pipe interfaces because they were still subject to Earth's gravity [43]. We cannot thus perfectly discriminate the actual effects of low-gravity fields from the redundant effects due to the additional stresses in our study.

To investigate the influence of freeze-thawing on the water permeability of lunar highlands soil, we also measured the water permeability of the lunar highlands regolith simulant LHS-1 after one freeze-thaw cycle. We measured the horizontal water permeability k_{xy} after defrosting as a reference measurement rather than the vertical water permeability at the simulated lunar gravity. This is because we primarily aim to investigate the influence of unique materials and angularity of lunar regolith particles on freeze-thaw and compare them with reported terrestrial soils while avoiding the influence of anisotropy on permeability. The porous media sample packed with the lunar regolith simulant, after its water permeability measurement prior to freeze, was cooled down to –20.0±0.3°C using a temperature-controlling freezer JCMC-310D (JCM Co., Ltd., Japan). The temperature of the given sample during freezing was continuously measured using a Pt100 temperature sensor and a data logger TR45 (T&D, Japan). The cooling rate between 18°C and the freezing point of water was approximately –40°C/h. The average cooling rate between the freezing point and –20°C was –4°C/h, roughly consistent with the observed variations in surface temperature at high lunar latitudes [45,46]. We kept the temperature of the given porous media sample constant at –20.0±0.3°C for 24 h, and after that, we defrosted it at room temperature of 18°C. We then measured the water permeability of the thawed sample by the following the same procedure we measured the water permeability of the sample before freezing.

3. Results

3.1. Water permeability k_{xy} of the studied granular materials

We measured the horizontal water permeability k_{xy} of the studied granular materials. The packing fraction η of the lunar highland regolith simulant LHS-1 we measured the water permeability was between 0.49 (49%) and 0.60 (60%), which ensured to appropriately measure the water permeability. The packing fraction of $\eta \leq 0.48$ was not successful in measuring the water permeability because we recognized particle movement within the sample column during the water permeability measurement. The sample column of lunar regolith simulant with packing fraction of $\eta \geq 0.61$ was not possible to make due to difficulties in packing the studied regolith simulant materials at such high packing fractions. The water permeability k_{xy} of lunar highland regolith simulant at packing fraction $\eta = 0.49$–0.60 ranged from 1.77×10^{-13} ($\pm$ 0.36×10^{-13}) m^2 to 5.53×10^{-13} ($\pm$ 0.22×10^{-13}) m^2 and generally decreased with higher packing fraction (Table 2 and Figure 3). In contrast, other fine silica sands and monodisperse spherical glass beads showed much higher water permeability (Figure 3). For example, the water permeabilities k_{xy} of fine silica sands T-7 at $\eta = 0.58$–0.62 and T-8 at $\eta = 0.55$–0.57 ranged from 1.02×10^{-11} ($\pm$ 0.18×10^{-11}) m^2 to 1.41×10^{-11} ($\pm$ 0.05×10^{-11}) m^2 and 3.73×10^{-12} ($\pm$ 0.06×10^{-12}) m^2 to 4.32×10^{-12} ($\pm$ 0.23×10^{-12}) m^2, respectively, indicating one to two orders of magnitudes higher than that of lunar highlands regolith simulant. The water permeability k_{xy} of monodisperse spherical glass beads BZ-01, having a median diameter similar to that of lunar highlands regolith, ranged from 1.09×10^{-11} ($\pm$ 0.01×10^{-11}) m^2 to 1.38×10^{-11} ($\pm$ 0.65×10^{-11}) m^2 at packing fraction $\eta =$ 0.65–0.67, revealing two orders of magnitudes higher than that of lunar highlands regolith simulant even at higher packing fractions (Figure 3). These results emphasize the considerably low water permeability of the lunar highland regolith simulant.

Table 2

Water permeability k_{xy} of lunar highlands regolith simulant LHS-1.

Packing fraction η	Water Permeability k_{xy} (m^2)
0.488	5.53×10^{-13} ($\pm$ 0.22×10^{-13})
0.500	3.93×10^{-13} ($\pm$ 0.12×10^{-13})
0.538	4.18×10^{-13} ($\pm$ 0.70×10^{-13})
0.550	3.23×10^{-13} ($\pm$ 0.13×10^{-13})
0.587	1.77×10^{-13} ($\pm$ 0.36×10^{-13})
0.600	2.00×10^{-13} ($\pm$ 0.22×10^{-13})

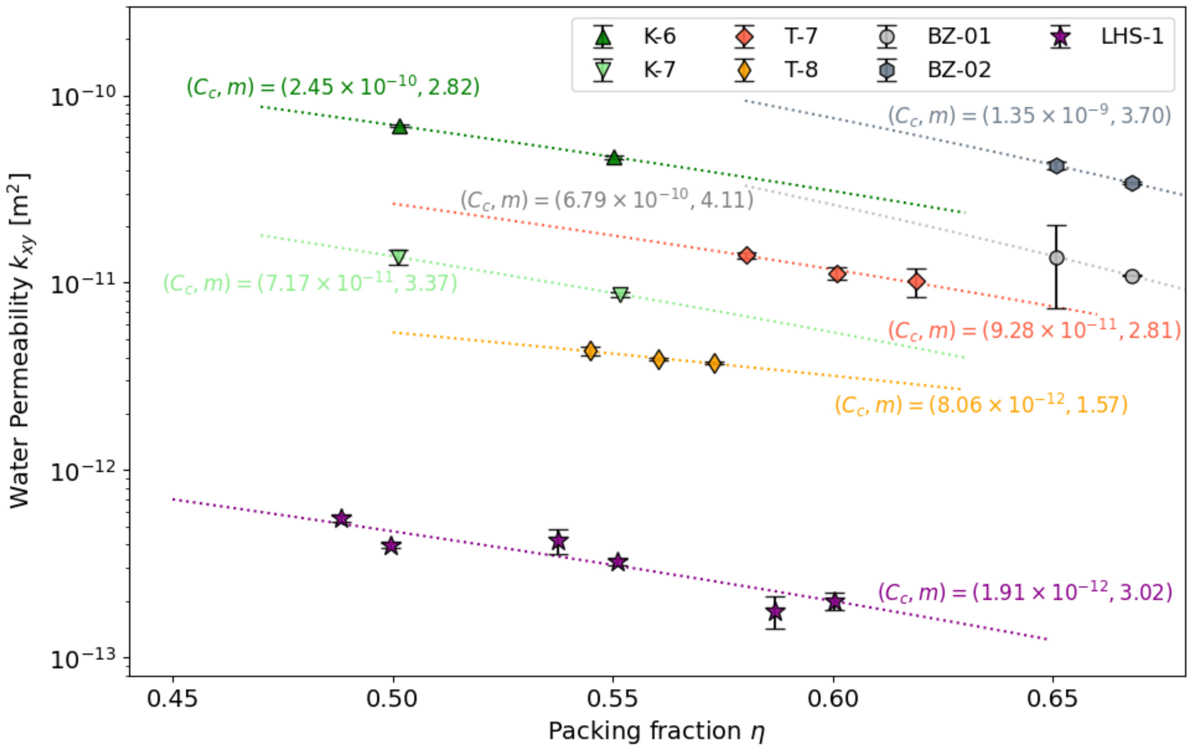

Figure 3
Water permeability k_{xy} of the studied granular materials without freeze-thaw.

3.2. Vertical water permeability k_z with different gravity fields

We estimated the vertical water permeability $k_z(g)$ of the given gravity field g by the tilting method (Figure 4). Our vertical water permeabilities of the glass beads BZ-01 and silica sands K-7 in the Earth's gravity field $k_z(g_e)$ were very close to the published data with the exact mean diameters [47]. The vertical water permeability of all the studied granular materials, including lunar highland regolith simulant LHS-1, was the lowest at simulated lunar gravity (0.17G) and increased with larger simulated gravity fields (Figure 4). The vertical water permeabilities of lunar highland regolith at the simulated lunar gravity field $k_z(0.17G)$ were 2.99×10^{-13} ($\pm 0.01\times10^{-13}$) m^2 and 1.57×10^{-13} ($\pm 0.01\times10^{-13}$) m^2 at packing fractions of $\eta = 0.54$ and $\eta = 0.59$, respectively, resulting in 83–97% and 49–61% of those at simulated Martian gravity field $k_z(0.38G)$ and Earth's gravity field $k_z(1G)$, respectively. In contrast, the difference between vertical water permeability at the simulated lunar gravity and larger gravity fields was more significant for silica sands and monodispersed spherical glass beads. The vertical water permeabilities at the simulated lunar gravity field $k_z(0.17G)$ of silica sands K-7 and monodispersed spherical glass beads BZ-01 were respectively 63% and 49% of those at the Martian gravity field $k_z(0.38G)$ and 36% and 28% of those at Earth's gravity field $k_z(1G)$. These results indicate that the vertical water permeability of lunar highland regolith may be less variable with different gravity fields than that of silica sands and spherical glass beads.

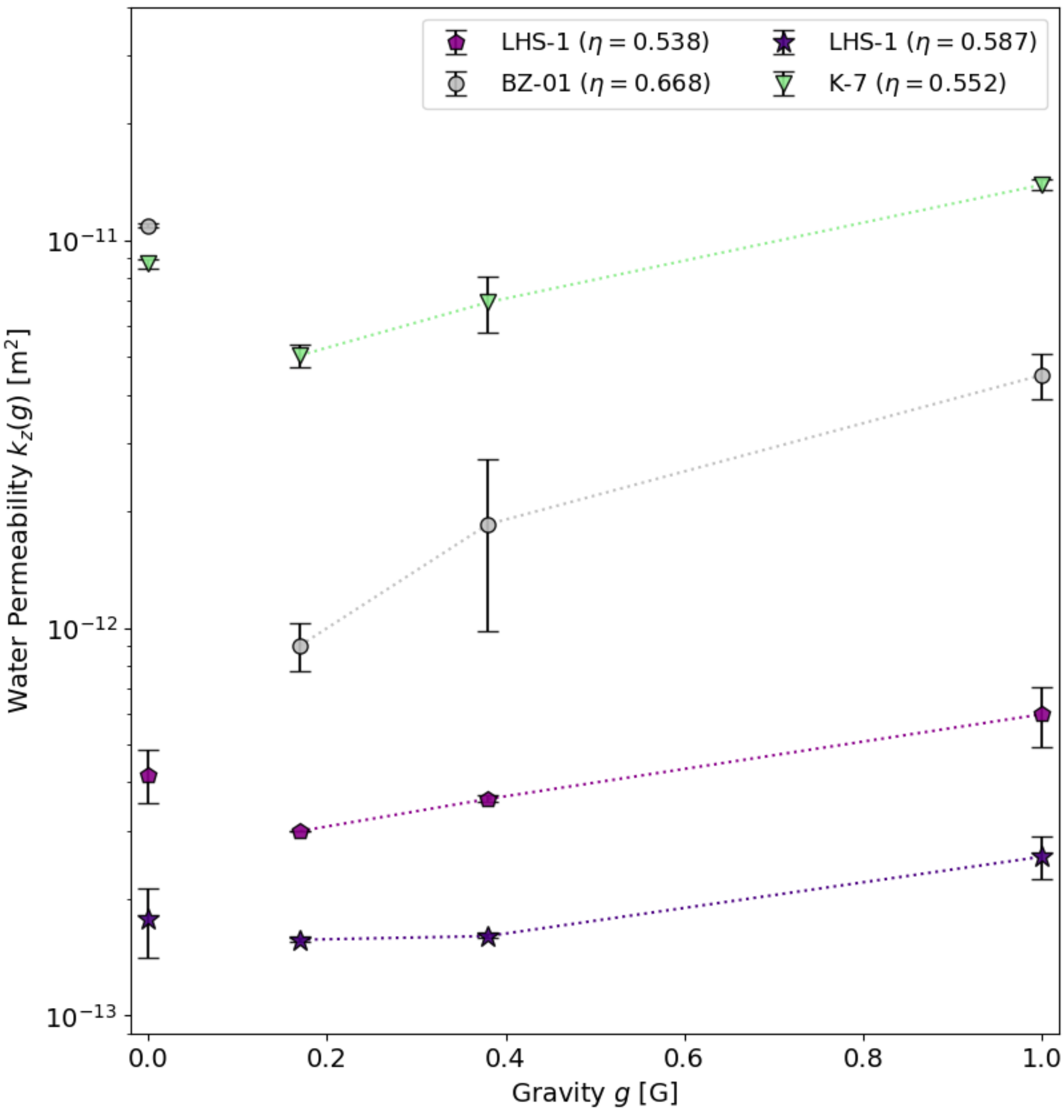

Figure 4

Vertical water permeability with different gravity fields $k_z(g)$. The vertical water permeability $k_z(0G)$ is identical to the horizontal water permeability k_{xy}.

3.3. Changes in water permeability after one freeze-thaw cycle

We also measured the water permeability k_{xy} of the lunar highlands regolith simulant LHS-1 after one freeze-thaw cycle. Likewise the water permeability before freezing k_{xy}^{unf} identical to the water permeability k_{xy} (Table 2 and Figure 3), the water permeability after one freeze-thaw cycle k_{xy}^{thw} decreased with a higher packing fraction η (Figure 5a). However, the water permeability after one freeze-thaw cycle of lunar highlands regolith k_{xy}^{thw}, ranging from 2.25×10^{-13} (± 0.19×10^{-13}) m^2 to 3.54×10^{-12} (± 0.96×10^{-12}) m^2 at packing fractions $\eta = 0.49$–0.59, was higher than that before freezing k_{xy}^{unf} at the given packing fraction η (Figure 5a). The ratio of water permeability $k_{xy}^{thw}/k_{xy}^{unf}$ resulted in relatively exponential decreases from 6.4 to 1.1 with packing fraction η, whereas the ratio was close to 1 at packing fractions of $\eta = 0.54$–0.59 (Figure 5b).

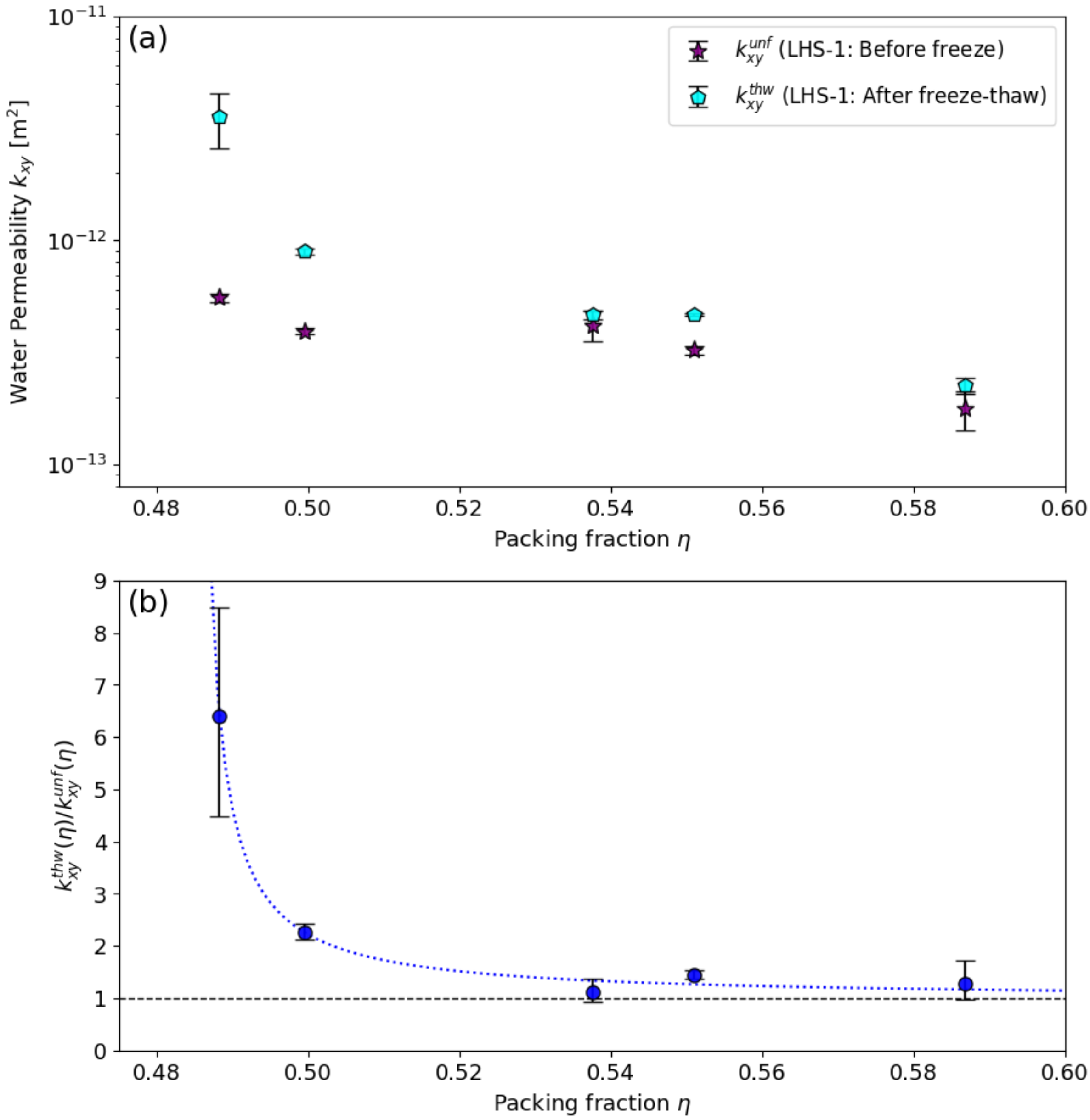

Figure 5

(a) Changes in water permeability of lunar highlands regolith before the freeze k_{xy}^{unf} [m^2] and water permeability after one freeze-thaw cycle k_{xy}^{thw} [m^2] with packing fraction η. Data of the water permeability k_{xy}^{unf} [m^2] are identical to the water permeability k_{xy} (Table 2 and Figure 3). (b) Changes in the ratio $k_{xy}^{thw}/k_{xy}^{unf}$ with packing fraction η.

4. Discussion

4.1. Low water permeability of lunar highland regolith and its implication

Our results revealed that the water permeability k_{xy} of lunar highland regolith simulant LHS-1 without freeze-thaw at packing fraction $\eta = 0.49$–0.60 was one to two orders of magnitude lower than that of fine silica sands and monodispersed spherical glass beads (Figure 3). Choate et al. [15] and LaMarche et al. [17] reported that the gas permeability of the top 25 cm of lunar soil from Surveyor 5 data and regolith simulant JSC-1A [17] is between 1×10^{-12} m^2 and 7×10^{-12} m^2 with a porosity $\phi = 0.3$–0.5. Thus, our water permeability of lunar highland regolith is about 15–20 times lower than the reported gas permeability, which is consistent with the fact that the gas permeability is generally several times to one order of magnitude higher than water permeability for Earth's soils [18]. Nevertheless, the low water permeability could be attributed to the small particle sizes of the lunar regolith. To assess whether the effect of particle size on the water permeability is significant, we describe the permeability in a more general form:

$$k \propto \phi^n \overline{D}^2 \qquad (3)$$

where $\overline{D}$ (m) is the average particle size and n is the exponent varying with porosities or packing fractions [48]. For example, from our measurements, the water permeability k_{xy} at a packing fraction $\eta = 0.55$ was 3.23×10^{-13} ($\pm$ 0.13×10^{-13}) m^2 for lunar highland regolith (Table 2). From Eq. (3), the water permeability of fine silica sands K-7 and T-8 at a packing fraction $\eta = 0.55$ could be $3.23\times10^{-13} \times (180/90)^2 = 1.3\times10^{-12}$ m^2 and $3.23\times10^{-13} \times (120/90)^2 = 5.7\times10^{-13}$ m^2, respectively, if the water permeability was predominantly dependent on porosity and grain size. However, our measured water permeabilities of fine silica sands K-7 and T-8 are respectively 6.7 and 70 times higher than these estimates (Figure 3). We would thus suggest that the water permeability of the surficial regolith layer in the lunar highlands, much lower than expected from particle size, is attributed to the morphology of regolith particles that comprises irregular and angular shape with sharp edges and micron-sized chunks due to the least weathering unlike Earth's soil particles (Figure 1). Furthermore, the lunar regolith comprises agglutinates, mostly glassy aggregates produced during the impact of micrometeorites into lunar soils [1]. The agglutinates are often very small with complex morphologies, which could make the water permeability lower than expected from our measurements.

It is thought that the water on the lunar surface is trapped within the interior of tiny lunar glasses in the soil that form out of the high heat generated by micrometeorite impacts [11,49,50]. The molecular water could also be hidden between regolith grains and within void spaces shielded from the harsh lunar environment [11]. However, due to the airless body, most water is subject to evaporation into space or redistribution to permanently shadowed regions. The abundance of molecular water per grain mass at the mid- to high-latitude of sunlit lunar surfaces results in 100–1000 μg/g (e.g., [11,12]), possessing significantly less than that retained in Earth's harsh deserts. We thus suggest that low water permeability of surficial regolith layer discourages water retention and drainage, perhaps somewhat encouraging to the low water abundance reported throughout the sunlit side of the Moon. The low water permeability is also essential to control mass wasting events on the lunar surface [51,52,53] because it can be one of the significant factors involving surface water and changing the mobility of regolith granular materials.

4.2. Water permeability at depths of the surficial regolith layer

Our results show that the water permeability k_{xy} of lunar highland regolith simulant decreases with higher packing fraction η and lower porosity ϕ (Figure 3). We thus expect that the water permeability of lunar regolith decreases with depth, leading to considerably lower values at deep depths within the surficial highland regolith layer than within the Earth's sediment column. Below, we estimate the water permeability-depth relationship within the surficial regolith layer. We obtain the possible water permeability-depth curve by using depth-porosity relationships reported in previous studies and the water permeability-porosity relationship that can be obtained from our results. The bulk density profile with depths of the surficial regolith layer is available from a few studies, including direct core sample measurements at the Apollo 15, 16, and 17 landing sites (e.g., [30]), Diviner radiometer observations [31], and Lunar Penetrating Radar at Chang'E-3 landing site [32]. The bulk density profile and grain density allow us to estimate the porosity-depth profile with depths (Figure 6a), although the profile can be variable with the locations of lunar highlands, lowlands, and Mare, and even landing sites and estimation methods. The porosity is estimated to be $\phi = 0.61$–0.75 at the lunar surface and $\phi = 0.32$–0.46 at a depth of 5 m within the surficial lunar regolith layer. The permeability k is expressed as a function of porosity or packing fraction:

$$k = C_c \frac{\phi^m}{1-\phi} = C_c \frac{(1-\eta)^m}{\eta}, \tag{4}$$

where C_c (m^2) is the Kozeny-coefficient like factor and m is the Archie exponent [54]. For example, the coefficients of water permeability k_{xy} of lunar regolith simulant were $(C_c, m) = (1.91\times10^{-12}, 3.02)$ from nonlinear square estimates. The Kozeny-coefficient like factor C_c of the lunar highlands regolith simulant LHS-1 was among the lowest in the studied granular materials (Figure 3). Using Eq. (4) and the vertical water permeability $k_z(g)$ of the lunar gravity field (Figure 4), we derive the water permeability-porosity relationships of the lunar highland regolith:

$$k_{lunar}(\phi) = k_{xy}\big(1 - exp(-a\eta)\big) = C_c \frac{\phi^m}{1-\phi}\big(1 - exp\big(-a(1-\phi)\big)\big) \tag{5}$$

where a is the positive coefficient that can be computed from the nonlinear least-square estimates of the vertical water permeability $k_z(g)$ of the lunar gravity field. We can finally obtain the water permeability-porosity curves of the lunar highlands regolith $k_{lunar}(z)$ by substituting the depth-porosity relationship to Eq. (5):

$$k_{lunar}(z) = C_c \frac{\phi(z)^m}{1-\phi(z)}\Big(1 - exp\Big(-a\big(1 - \phi(z)\big)\Big)\Big) \tag{6}$$

where z (m) is the depth below the lunar surface.

Using Eq. (6), the water permeability of the surficial regolith layer in the lunar highlands $k_{lunar}(z)$ results in a relatively rapid drop at the upper ~1 m of regolith layer and decreases with increasing depth below a depth of 2–4 m (Figure 6b). The water permeability $k_{lunar}(z)$ is 6×10^{-13}–2×10^{-12} m^2 at the lunar surface, whereas it declines to 7×10^{-14}–3×10^{-13} m^2 at a depth of 5 m within the surficial lunar regolith layer. The influence of the lunar gravity on the water permeability should be further investigated in future studies by laboratory and lunar missions; however, the values of water permeability at 5 m depth of lunar highland regolith are comparable to the permeabilities at much greater depths of 50 – 100 m and 300 – 600 m for Earth's oceanic crust and continental crust, respectively [55,56], highlighting the considerable low permeability of surficial lunar highland regolith. Although we only estimate the water permeability-depth profile of lunar highland regolith, our study will provide a wide range of further research with different lunar regions (e.g., highlands, lowlands, Mare) and different properties of regolith particles.

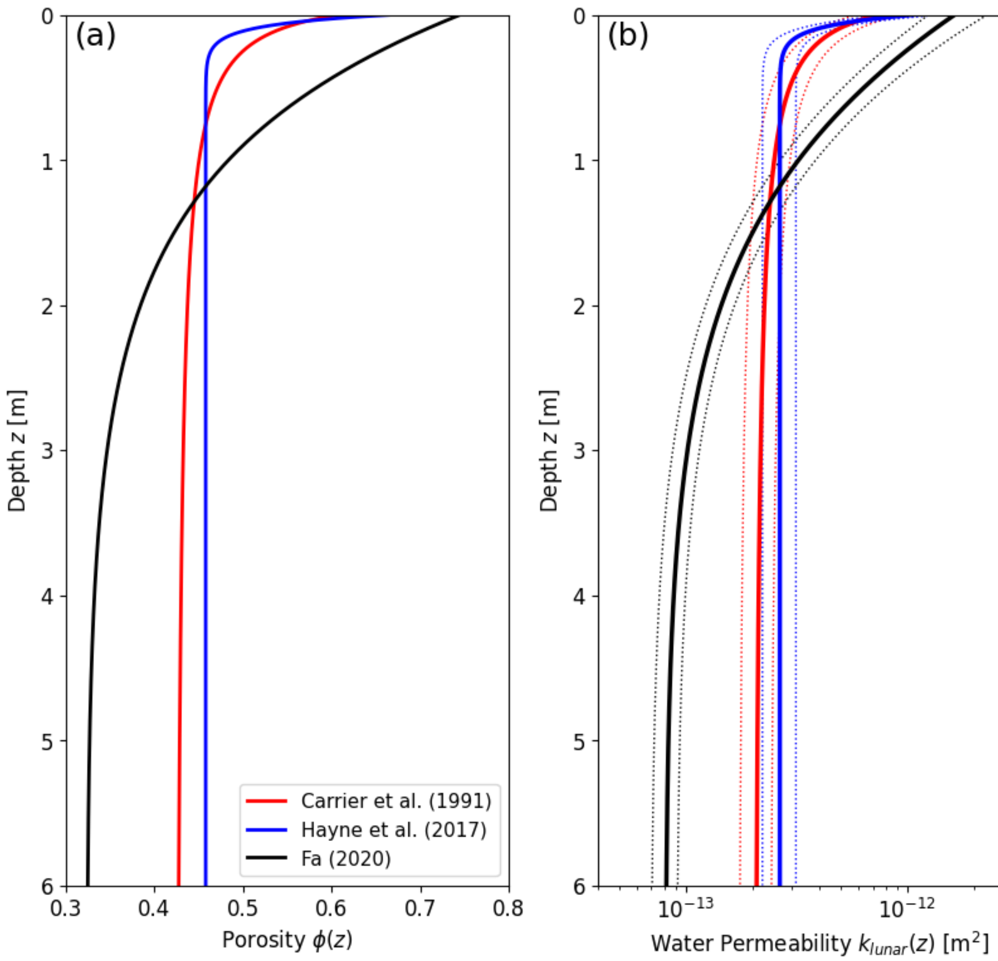

Figure 6
(a) Porosity of the lunar regolith as a function of depth. Red, blue, and black solid curves are derived from the bulk density profiles reported by direct core sample measurements at the Apollo 15, 16, 17 landing sites [30], Diviner radiometer observations [31], and Lunar Penetrating Radar at Chang'E-3 landing site [32], respectively. (b) Water permeability of the lunar regolith $k_{lunar}(z)$ as a function of depth z. Red, blue, and black curves are computed by using bulk density profiles reported in Carrier et al. [30], Hayne et al. [31], and Fa [32], respectively, and our porosity-water permeability relationship in Eq. (6).

Our studies undoubtedly indicated that the water permeability of lunar highland regolith is at least one to two orders of magnitudes lower than fine silica sands and monodisperse spherical glass beads at the given packing fraction (Figure 3). We further investigated the vertical water permeability $k_z(g)$ at the given gravity field g using the tilting method (Figure 4) to estimate the first-ever water permeability-depth relationship within the surficial regolith layer (Figure 6), as discussed above. In this paper, we used the tilting method because it is the only method currently available to produce very long-duration, continuous, and steady water flow, and stable and controllable low gravitational fields, all essential to the water permeability measurement (Section 2.2). Here, we recognize that our results of the vertical water permeability $k_z(g)$ in the given gravity field g should not be taken as definitive due to potential uncertainty in the tilting method used in our measurements. For instance, our tilting method might generate unwanted additional stresses to the "actual" water flow by friction and lateral stresses on the interfaces of water-regolith, water-pipe, and regolith-pipe because they were still subject to Earth's gravity [43]. This makes our estimated permeability values challenging to completely differentiate between the actual effects of low-gravity fields and the unwanted effects of the additional stresses. However, the ratio of zero-gravity "vertical" water permeability to the vertical permeability in the Earth's gravity field $k_{xy}/k_z(g_e)$ was lower than 1.0, yielding 0.70, 0.69, and 0.63 for the lunar highland regolith ($\eta = 0.54$ and $\eta = 0.59$) and silica sand K-7 ($\eta = 0.55$), respectively, most likely representing the actual changes in the connectivity of pore spaces and the resulting water flow at the given fixed packing fraction [36] more than the effect due to the additional stresses. Moreover, all the studied granular materials showed that the ratio $k_z(0.17G)/k_z(g_e)$ is lower than $k_z(0.38G)/k_z(g_e)$, indicating the ratio $k_z(g)/k_z(g_e)$ is lower with a lower gravity field g (Figure 4). These results of $k_{xy}/k_z(g_e)$ and $k_z(g)/k_z(g_e)$ could suggest that our method appropriately represents variable degrees of interconnected pore spaces and/or water flow along with variable gravity fields g. Also, our vertical water permeabilities of the glass beads BZ-01 and silica sands K-7 in the Earth's gravity field $k_z(g_e)$ are close to the published data with the exact mean diameters [47]. All these results could thus ensure the validation of our water permeability measurements. Our first estimation of the water permeability-depth relationship within the surficial regolith layer could be an alternative clue for the presence and abundance of the molecular water; however, a more reliable water permeability-depth relationship can be provided when alternative methods, in-situ measurements, and more porosity data are made available by future studies.

4.3. Influences of freeze-thaw on water permeability of lunar highland regolith

The vertical water permeabilities $k_z(g)$ with any studied packing fractions showed their minimum in the simulated lunar gravity environment (0.17G). The vertical permeability of the lunar highland regolith simulant was 1.57×10^{-13} ($\pm$ 0.01×10^{-13}) m^2 at a packing fraction $\eta = 0.59$. In contrast, the vertical water permeability in the simulated gravity field 0.17G –1.00G increased as the simulated gravity field increased (Figure 4). This is likely because the higher gravity field increases the contact surface area between regolith particles and reduces the horizontal fluid paths when the porosity is unchanged. It accommodates more spaces in a gravitational direction for water flow, leading to reducing tortuosity. We also found that the water permeability after one freeze-thaw cycle of lunar highlands regolith k_{xy}^{thw} is higher than that before freezing k_{xy}^{unf} at the given packing fraction η and that the ratio $k_{xy}^{thw}/k_{xy}^{unf}$ is more significant with lower packing fractions η. Freezing of water-bearing soils accompanies phase change, migration, and freezing expansion of water, which significantly influence the homogeneity of porous media structure and water distribution. The permeability of fine-grained glacial till and loess on the Earth generally increases 1.1 to 1.2 times after one freeze-thaw cycle when packing fraction $\eta \geq 0.58$ [14,57], which is consistent with our results of lunar highland regolith. Therefore, we would attribute our findings to the fact that the pore water in the solid phase due to freezing allowed the rearrangement of the loosely packed regolith particles and changed the total contact area between the regolith particles. The presence of agglutinates can also influence the rearrangement of the packed regolith particles due to the freeze-thaw. Anyhow, the amount of water that could be present within pore spaces of the given regolith column is more significant when the packing fraction η is smaller, and water in the void spaces determines the required energy to move the system toward the loosed packing configuration after defrosting [58]. We would thus expect that the regolith on the sunlit lunar surface may have higher permeability than that shown in this study, given that the sunlit lunar surface should have been subject to multiple freeze-thaw cycles, although further studies are necessary to examine the hypothesis.

Below, we estimate changes in the tortuosity of lunar highland regolith after one freeze-thaw cycle. The Kozeny-Carman relationship is widely used to relate permeability, porosity and tortuosity in the circular section pipes we studied. The Kozeny-Carman equation is given by:

$$k = C_{kc}\frac{\phi^3}{(1-\phi)^2\tau^2}d^2 \tag{7}$$

where τ is the tortuosity of the porous media sample column filled with lunar highlands regolith, d (m) is the diameter of regolith particles, and C_{kc} is the Kozeny-Carman coefficient. Here, the tortuosity τ (e.g., [59]) is defined by the ratio of the total flow-path length within packed regolith porous media to the length of the sample column (200 mm). The Kozeny-Carman relation in Eq. (7) can be extended to the granular system with mixed particle sizes by using an average particle size:

$$k = C_{kc}\frac{\phi^3}{(1-\phi)^2\tau^2}\overline{D}^2 \tag{8}$$

where $\overline{D}$ is the average particle size of the granular system [48]. To investigate changes in tortuosity due to freeze-thaw, we compute the tortuosity ratio k_{thw}/k_{unf} using Eq. (8), where k_{unf} and k_{thw} are the horizontal water permeability before and after one freeze-thaw cycle, respectively. The tortuosity ratio τ_{thw}/τ_{unf} of lunar highland regolith due to freeze-thaw, where τ_{unf} and τ_{thw} are the tortuosity before and after one freeze-thaw cycle, increases exponentially with higher packing fraction. The ratio yields $\tau_{thw}/\tau_{unf} =$ 0.40(+0.08/–0.05) and $\tau_{thw}/\tau_{unf} =$ 0.89(+0.13/–0.12) at packing fraction of $\eta = 0.49$ and $\eta = 0.59$, respectively (Figure 7). This indicates that the tortuosity of the loosely packed lunar highland regolith particles with a packing fraction of $\eta = 0.49$ (porosity of $\phi = 0.51$) decreases by about 60% due to one freeze-thaw cycle, suggesting that freeze-thaw at the upper ~1 m of surficial regolith layer with low porosity (Figure 6a) can contribute to a significant reduction in the total flow path within the porous regolith media column.

Water-rich permafrost is thought to exist in the cold subsurface of the Moon [60,61]. Increasing subsurface permeability due to tortuosity reduction may alter possible subsurface water recharge mediated by permafrost thawing, leading to an increase in dissolved minerals and materials transportation as on the Earth [62]. Also, the permafrost active layer [63,64,65], the upper meter(s)-thick layer of the underground undergoing a freeze-thaw cycle perhaps shorter than Earth's cycle, could be present in the lunar subsurface due to considerable variations in surface temperature between lunar day and night time [45,46]. Thus, the changes in the water permeability of the surficial regolith layer due to freeze-thaw cycles could also alter the sensitivity to temperature changes and shift the thawing front and the frost table within possible permafrost and active layers, as seen on the Earth [63,66,67].

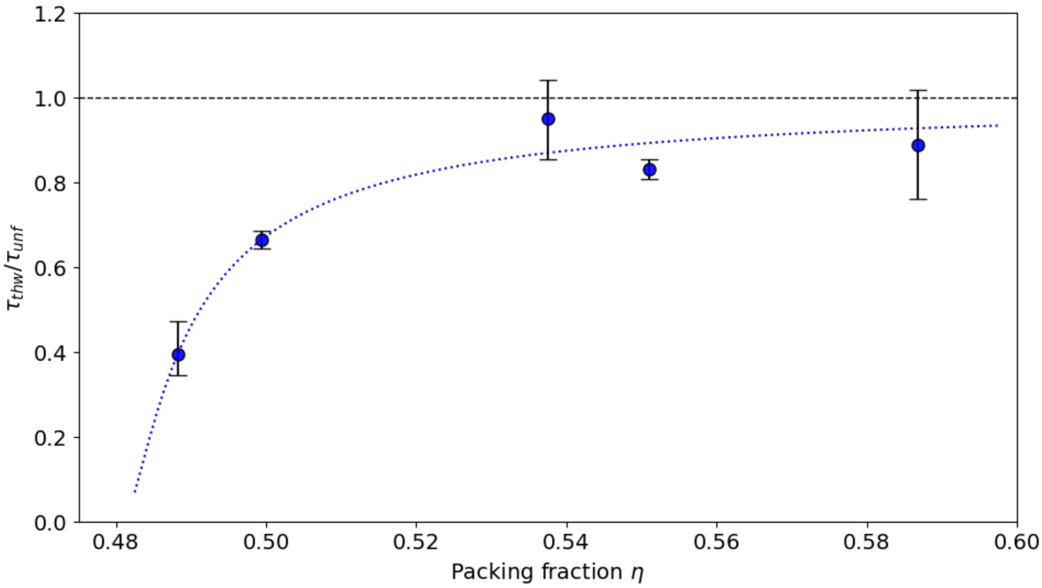

Figure 7
Changes in the tortuosity ratio τ_{thw}/τ_{unf} of lunar highlands regolith filled in the studied porous media sample column.

5. Conclusions

We investigated the water permeability of lunar highland regolith and its change due to freeze-thaw using the high-fidelity Lunar highlands regolith simulant LHS-1. We measured the water permeability by applying Darcy's law to the porous media sample column filled with the regolith simulant LHS-1 at various packing fractions and the tilting method to simulate the lunar gravitational field. Our results indicated that the water permeability of lunar highland regolith is at least one to two orders of magnitudes lower than that of fine silica sands and monodisperse spherical glass beads at the given packing fraction. We concluded that such low water permeability of lunar highland regolith is attributed to the morphology of regolith particles comprising irregular and angular shapes with sharp edges and micron-sized chunks due to the least weathering, unlike soil grains on the Earth. The vertical water permeability $k_z(g)$ of lunar highland regolith simulant is 1.57×10^{-13} ($\pm$ 0.01×10^{-13}) m^2 at a packing fraction $\eta = 0.59$. It should be noted that our estimated permeability values might be subject to the redundant effects of the additional stresses due to Earth's gravity other than the actual effects of low-gravity fields, and further studies are thus necessary to investigate the influence of low-gravity on water permeability. However, the vertical water permeabilities with any studied packing fractions show their minimum in the simulated lunar gravity environment (0.17G). This is because the higher gravity increases the total contact area between regolith particles and decreases tortuosity. Using the porosity-depth relationship estimated from earlier studies, we obtained the water permeability-depth relationship within the surficial lunar regolith layer. The vertical water permeability is 6×10^{-13}–2×10^{-12} m^2 at the lunar surface and it declines to 7×10^{-14}–3×10^{-13} m^2 at a depth of 5 m within the surficial regolith layer, although more porosity data and further measurements are necessary. We also found that the water permeability of lunar highland regolith simulant increased after one freeze-thaw cycle, achieving 6.4 times higher than the permeability before the freeze, and the increase was more significant with lower packing fractions. We attribute this finding to the fact that the pore water in the solid phase due to freezing encouraged the rearrangement of the regolith particles and changed the total contact area between the particles. Our results of the water permeability of lunar highland regolith simulant will advance a better understanding of the abundance and distribution of molecular water on the lunar surface, lunar surface processes, and broad areas of the engineering and agricultural applications of regolith utilizations.

CRediT authorship contribution statement
Yoshiki Tabuchi: Conceptualization, Data curation, Formal analysis, Investigation, Methodology, Validation, Visualization, Writing – review & edit.
Arata Kioka: Conceptualization, Data curation, Formal analysis, Funding acquisition, Methodology, Project administration, Resources, Supervision, Validation, Visualization, Writing – original draft, Writing – review & edit.
Yasuhiro Yamada: Resources.

Declaration of Competing Interest

The authors declare that they have no known competing financial interests or personal relationships that could have appeared to influence the work reported in this paper.

Acknowledgements

The authors thank N. Yamamoto and A. Shishida for assisting SEM measurements and sample preparations. The authors also thank the reviewers for their valuable comments. This work was supported by the JSPS Bilateral Joint Research Project (JPJSBP120214811) and JSPS KAKENHI Grant-in-Aid for Early-Career Scientists (JP23K13698).

References

1. P. Lucey, R.L. Korotev, J.J. Gillis, L.A. Taylor, D. Lawrence, B.A. Campbell, R. Elphic, B. Feldman, L.L. Hood, D. Hunten, M. Mendillo, S. Noble, J.J. Papike, R.C. Reedy, S. Lawson, T. Prettyman, O. Gasnault, S. Maurice, Understanding the Lunar Surface and Space-Moon Interactions, Rev. Mineral. Geochem. 60 (2006) 83–219. https://doi.org/10.2138/rmg.2006.60.2.
2. V.R. Oberbeck, W.L. Quaide, Estimated thickness of a fragmental surface layer of Oceanus Procellarum, J. Geophys. Res. 72 (1967) 4697–4704. https://doi.org/10.1029/JZ072i018p04697.
3. Y. Shkuratov, N. V. Bondarenko, Regolith Layer Thickness Mapping of the Moon by Radar and Optical Data, Icarus 149 (2001) 329–338. https://doi.org/10.1006/icar.2000.6545.
4. W. Fa, M.A. Wieczorek, Regolith thickness over the lunar nearside: Results from Earth-based 70-cm Arecibo radar observations, Icarus 218 (2012) 771–787. https://doi.org/10.1016/j.icarus.2012.01.010.
5. D. Schulze-Makuch, I.A. Crawford, Was There an Early Habitability Window for Earth's Moon?, Astrobiology 18 (2018) 985–988. https://doi.org/10.1089/ast.2018.1844.
6. B.A. Lomax, M. Conti, N. Khan, N.S. Bennett, A.Y. Ganin, M.D. Symes, Proving the viability of an electrochemical process for the simultaneous extraction of oxygen and production of metal alloys from lunar regolith, Planet. Space Sci. 180 (2020) 104748. https://doi.org/10.1016/j.pss.2019.104748.
7. K. Wang, P.N. Lemougna, Q. Tang, W. Li, X. Cui, Lunar regolith can allow the synthesis of cement materials with near-zero water consumption, Gondwana Res. 44 (2017) 1–6. https://doi.org/10.1016/j.gr.2016.11.001.
8. A.G. Caporale, M. Palladino, S. De Pascale, L.G. Duri, Y. Rouphael, P. Adamo, How to make the Lunar and Martian soils suitable for food production - Assessing the changes after manure addition and implications for plant growth, J. Environ. Manage. 325 (2023) 116455. https://doi.org/10.1016/j.jenvman.2022.116455.
9. S. Li, P.G. Lucey, R.E. Milliken, P.O. Hayne, E. Fisher, J.-P. Williams, D.M. Hurley, R.C. Elphic, Direct evidence of surface exposed water ice in the lunar polar regions, Proc. Natl. Acad. Sci. 115 (2018) 8907–8912. https://doi.org/10.1073/pnas.1802345115.
10. C.I. Honniball, P.G. Lucey, C.M. Ferrari ‐ Wong, A. Flom, S. Li, H.M. Kaluna, D. Takir, Telescopic Observations of Lunar Hydration: Variations and Abundance, J. Geophys. Res. Planets 125 (2020) e2020JE006484. https://doi.org/10.1029/2020JE006484.
11. C.I. Honniball, P.G. Lucey, S. Li, S. Shenoy, T.M. Orlando, C.A. Hibbitts, D.M. Hurley, W.M. Farrell, Molecular water detected on the sunlit Moon by SOFIA, Nat. Astron. 5 (2021) 121–127. https://doi.org/10.1038/s41550-020-01222-x.
12. H. He, J. Ji, Y. Zhang, S. Hu, Y. Lin, H. Hui, J. Hao, R. Li, W. Yang, H. Tian, C. Zhang, M. Anand, R. Tartèse, L. Gu, J. Li, D. Zhang, Q. Mao, L. Jia, X. Li, Y. Chen, L. Zhang, H. Ni, S. Wu, H. Wang, Q. Li, H. He, X. Li, F. Wu, A solar wind-derived water reservoir on the Moon hosted by impact glass beads, Nat. Geosci. 16 (2023) 294–300. https://doi.org/10.1038/s41561-023-01159-6.
13. E.J. Chamberlain, A.J. Gow, Effect of freezing and thawing on the permeability and structure of soils, Eng. Geol. 13 (1979) 73–92. https://doi.org/10.1016/0013-7952(79)90022-X.
14. P. Viklander, Permeability and volume changes in till due to cyclic freeze/thaw, Can. Geotech. J. 35 (1998) 471–477. https://doi.org/10.1139/t98-015.
15. R. Choate, S.A. Batterson, E.M. Christensen, R.E. Hutton, J.D. Jaffe, R.H. Jones, H.Y. Ko, R.L. Spencer, F.B. Sperling, G.H. Sutton, G.H., Lunar surface mechanical properties. In: Surveyor Project. Part 1: Project Description and Performance. JPL Technical Report 32-1265. Jet Propulsion Laboratory, Pasadena, 1968.
16. H.G. Sizemore, M.T. Mellon, Laboratory characterization of the structural properties controlling dynamical gas transport in Mars-analog soils, Icarus 197 (2008) 606–620. https://doi.org/10.1016/j.icarus.2008.05.013.
17. C.Q. LaMarche, J.S. Curtis, P.T. Metzger, Permeability of JSC-1A: A lunar soil simulant, Icarus 212 (2011) 383–389. https://doi.org/10.1016/j.icarus.2010.12.015.
18. W. Tanikawa, T. Shimamoto, Comparison of Klinkenberg-corrected gas permeability and water permeability in sedimentary rocks, Int. J. Rock Mech. Min. Sci. 46 (2009) 229–238. https://doi.org/10.1016/j.ijrmms.2008.03.004.

19. M. Anand, I.A. Crawford, M. Balat-Pichelin, S. Abanades, W. van Westrenen, G. Péraudeau, R. Jaumann, W. Seboldt, A brief review of chemical and mineralogical resources on the Moon and likely initial in situ resource utilization (ISRU) applications, Planet. Space Sci. 74 (2012) 42–48. https://doi.org/10.1016/j.pss.2012.08.012.
20. J.N. Rasera, J.J. Cilliers, J.A. Lamamy, K. Hadler, The beneficiation of lunar regolith for space resource utilisation: A review, Planet. Space Sci. 186 (2020) 104879. https://doi.org/10.1016/j.pss.2020.104879.
21. L.G. Duri, A.G. Caporale, Y. Rouphael, S. Vingiani, M. Palladino, S. De Pascale, P. Adamo, The Potential for Lunar and Martian Regolith Simulants to Sustain Plant Growth: A Multidisciplinary Overview, Front. Astron. Sp. Sci. 8 (2022). https://doi.org/10.3389/fspas.2021.747821.
22. J.E. Richardson, O. Abramov, Modeling the Formation of the Lunar Upper Megaregolith Layer, Planet. Sci. J. 1 (2020) 2. https://doi.org/10.3847/PSJ/ab7235.
23. A.R. Clendenen, A. Aleksandrov, B.M. Jones, P.G. Loutzenhiser, D.T. Britt, T.M. Orlando, Temperature programmed desorption comparison of lunar regolith to lunar regolith simulants LMS-1 and LHS-1, Earth Planet. Sci. Lett. 592 (2022) 117632. https://doi.org/10.1016/j.epsl.2022.117632.
24. M. Isachenkov, S. Chugunov, Z. Landsman, I. Akhatov, A. Metke, A. Tikhonov, I. Shishkovsky, Characterization of novel lunar highland and mare simulants for ISRU research applications, Icarus 376 (2022) 114873. https://doi.org/10.1016/j.icarus.2021.114873.
25. J.M. Long-Fox, Z.A. Landsman, P.B. Easter, C.A. Millwater, D.T. Britt, Geomechanical properties of lunar regolith simulants LHS-1 and LMS-1, Adv. Sp. Res. (2023). https://doi.org/10.1016/j.asr.2023.02.034.
26. K.T. O'Neill, E.O. Fridjonsson, D. Smeed, T.A.J. Hopper, M.L. Johns, Characterising water in Lunar and Martian regolith materials using nuclear magnetic resonance, Icarus 399 (2023) 115544. https://doi.org/10.1016/j.icarus.2023.115544.
27. K. Yin, Z. Cheng, J. Liu, A. Chen, Shear properties of LHS-1 and LMS-1 Lunar regolith simulants, Planet. Space Sci. 226 (2023) 105630. https://doi.org/10.1016/j.pss.2022.105630.
28. E. Kossel, C. Deusner, N. Bigalke, M. Haeckel, The Dependence of Water Permeability in Quartz Sand on Gas Hydrate Saturation in the Pore Space, J. Geophys. Res. Solid Earth. 123 (2018) 1235–1251. https://doi.org/10.1002/2017JB014630.
29. F.B. Wadsworth, C.E.J. Vossen, D. Schmid, M. Colombier, M.J. Heap, B. Scheu, D.B. Dingwell, Determination of permeability using a classic Darcy water column, Am. J. Phys. 88 (2020) 20–24. https://doi.org/10.1119/10.0000296.
30. W.D. Carrier, G.R. Olhoeft, W. Mendell, Physical properties of the lunar surface, in: G.H. Heiken, D.T. Vaniman, B.M. French (Eds.), Lunar source book: A user's guide to the Moon, Cambridge University Press, New York, 1991, pp. 530–552.
31. P.O. Hayne, J.L. Bandfield, M.A. Siegler, A.R. Vasavada, R.R. Ghent, J.-P. Williams, B.T. Greenhagen, O. Aharonson, C.M. Elder, P.G. Lucey, D.A. Paige, Global Regolith Thermophysical Properties of the Moon From the Diviner Lunar Radiometer Experiment, J. Geophys. Res. Planets 122 (2017) 2371–2400. https://doi.org/10.1002/2017JE005387.
32. W. Fa, Bulk Density of the Lunar Regolith at the Chang'E-3 Landing Site as Estimated From Lunar Penetrating Radar, Earth Sp. Sci. 7 (2020). https://doi.org/10.1029/2019EA000801.
33. M. Nakagawa, A. Kioka, K. Tagomori, Nanobubbles as friction modifier, Tribol. Int. 165 (2022) 107333. https://doi.org/10.1016/j.triboint.2021.107333.
34. J. Cooper, R. Dooley, Release on the IAPWS formulation 2008 for the viscosity of ordinary water substance, Int. Assoc. Prop. Water Steam (2008) 1–9.
35. P.N. Dwivedi, S.N. Upadhyay, Particle-Fluid Mass Transfer in Fixed and Fluidized Beds, Ind. Eng. Chem. Process Des. Dev. 16 (1977) 157–165. https://doi.org/10.1021/i260062a001.
36. R. A. Freeze, J. A. Cherry, Groundwater, Prentice-Hall, 1979.
37. R. Li, G. Zhou, K. Yan, J. Chen, D. Chen, S. Cai, P.-Q. Mo, Preparation and characterization of a specialized lunar regolith simulant for use in lunar low gravity simulation, Int. J. Min. Sci. Technol. 32 (2022) 1–15. https://doi.org/10.1016/j.ijmst.2021.09.003.
38. W.W. Boles, W.D. Scott, J.F. Connolly, Excavation Forces in Reduced Gravity Environment, J. Aerosp. Eng. 10 (1997) 99–103. https://doi.org/10.1061/(ASCE)0893-1321(1997)10:2(99).

39. H.H. Bui, T. Kobayashi, R. Fukagawa, J.C. Wells, Numerical and experimental studies of gravity effect on the mechanism of lunar excavations, J. Terramechanics 46 (2009) 115–124. https://doi.org/10.1016/j.jterra.2009.02.006.
40. P.G. Hofmeister, J. Blum, D. Heiβelmann, The Flow Of Granular Matter Under Reduced-Gravity Conditions, AIP Conf. Proc. 1145 (2009) 71–74. https://doi.org/10.1063/1.3180028.
41. Y. Huang, C. Zhu, X. Xiang, W. Mao, Liquid-Gas-Like Phase Transition in Sand Flow Under Microgravity, Microgravity Sci. Technol. 27 (2015) 155–170. https://doi.org/10.1007/s12217-015-9424-2.
42. M. Krause, J. Blum, Growth and Form of Planetary Seedlings: Results from a Sounding Rocket Microgravity Aggregation Experiment, Phys. Rev. Lett. 93 (2004) 021103. https://doi.org/10.1103/PhysRevLett.93.021103.
43. M. Zou, S. Fan, R. Shi, Y. Yang, J. Li, Effect of gravity on the mechanical properties of lunar regolith tested using a low gravity simulation device, J. Terramechanics 60 (2015) 11–22. https://doi.org/10.1016/j.jterra.2015.04.003.
44. D. Liu, T. Zeng, L. Wang, G. Mo, J. Li, Q. Sun, J. Gong, Research of Reinforcement Deployment Mechanism of Automatic Sampler for Lunar Sample Return Mission, IOP Conf. Ser. Earth Environ. Sci. 781 (2021) 022047. https://doi.org/10.1088/1755-1315/781/2/022047.
45. J.-P. Williams, D.A. Paige, B.T. Greenhagen, E. Sefton-Nash, The global surface temperatures of the Moon as measured by the Diviner Lunar Radiometer Experiment, Icarus 283 (2017) 300–325. https://doi.org/10.1016/j.icarus.2016.08.012.
46. X. Xiao, S. Yu, J. Huang, H. Zhang, Y. Zhang, L. Xiao, Thermophysical properties of the regolith on the lunar far side revealed by the in situ temperature probing of the Chang'E-4 mission, Natl. Sci. Rev. 9 (2022). https://doi.org/10.1093/nsr/nwac175.
47. M. Kimura, Prediction of tortuosity, permeability, and pore radius of water-saturated unconsolidated glass beads and sands, J. Acoust. Soc. Am. 143 (2018) 3154–3168. https://doi.org/10.1121/1.5039520.
48. G. Mavko, T. Mukerji, J. Dvorkin, The Rock Physics Handbook, Cambridge University Press, 2009. https://doi.org/10.1017/CBO9780511626753.
49. R.T. Daly, P.H. Schultz, The delivery of water by impacts from planetary accretion to present, Sci. Adv. 4 (2018). https://doi.org/10.1126/sciadv.aar2632.
50. M. Benna, D.M. Hurley, T.J. Stubbs, P.R. Mahaffy, R.C. Elphic, Lunar soil hydration constrained by exospheric water liberated by meteoroid impacts, Nat. Geosci. 12 (2019) 333–338. https://doi.org/10.1038/s41561-019-0345-3.
51. Z. Xiao, Z. Zeng, N. Ding, J. Molaro, Mass wasting features on the Moon – how active is the lunar surface?, Earth Planet. Sci. Lett. 376 (2013) 1–11. https://doi.org/10.1016/j.epsl.2013.06.015.
52. B.P. Kokelaar, R.S. Bahia, K.H. Joy, S. Viroulet, J.M.N.T. Gray, Granular avalanches on the Moon: Mass-wasting conditions, processes, and features, J. Geophys. Res. Planets 122 (2017) 1893–1925. https://doi.org/10.1002/2017JE005320.
53. V.T. Bickel, S. Loew, J. Aaron, N. Goedhart, A Global Perspective on Lunar Granular Flows, Geophys. Res. Lett. 49 (2022). https://doi.org/10.1029/2022GL098812.
54. A. Costa, Permeability-porosity relationship: A reexamination of the Kozeny-Carman equation based on a fractal pore-space geometry assumption, Geophys. Res. Lett. 33 (2006) L02318. https://doi.org/10.1029/2005GL025134.
55. C.E. Manning, S.E. Ingebritsen, Permeability of the continental crust: Implications of geothermal data and metamorphic systems, Rev. Geophys. 37 (1999) 127–150. https://doi.org/10.1029/1998RG900002.
56. X. Kuang, J.J. Jiao, An integrated permeability-depth model for Earth's crust, Geophys. Res. Lett. 41 (2014) 7539–7545. https://doi.org/10.1002/2014GL061999.
57. J. Xu, Y. Li, C. Ren, S. Wang, S.K. Vanapalli, G. Chen, Influence of freeze-thaw cycles on microstructure and hydraulic conductivity of saline intact loess, Cold Reg. Sci. Technol. 181 (2021) 103183. https://doi.org/10.1016/j.coldregions.2020.103183.
58. M. Pakpour, N. Vandewalle, G. Lumay, Decompaction of wet granular materials under freeze-thaw cycling, Phys. Rev. E. 99 (2019) 012901. https://doi.org/10.1103/PhysRevE.99.012901.

59. B. Ghanbarian, A.G. Hunt, R.P. Ewing, M. Sahimi, Tortuosity in Porous Media: A Critical Review, Soil Sci. Soc. Am. J. 77 (2013) 1461–1477. https://doi.org/10.2136/sssaj2012.0435.
60. I. Mitrofanov, M. Litvak, A. Sanin, A. Malakhov, D. Golovin, W. Boynton, G. Droege, G. Chin, L. Evans, K. Harshman, F. Fedosov, J. Garvin, A. Kozyrev, T. McClanahan, G. Milikh, M. Mokrousov, R. Starr, R. Sagdeev, V. Shevchenko, V. Shvetsov, V. Tret'yakov, J. Trombka, A. Varenikov, A. Vostrukhin, Testing polar spots of water-rich permafrost on the Moon: LEND observations onboard LRO, J. Geophys. Res. Planets 117 (2012) E00H27. https://doi.org/10.1029/2011JE003956.
61. G. Kletetschka, J. Klokočník, N. Hasson, J. Kostelecký, A. Bezděk, K. Karimi, Distribution of water phase near the poles of the Moon from gravity aspects, Sci. Rep. 12 (2022) 4501. https://doi.org/10.1038/s41598-022-08305-x.
62. S. Ge, J. McKenzie, C. Voss, Q. Wu, Exchange of groundwater and surface-water mediated by permafrost response to seasonal and long term air temperature variation, Geophys. Res. Lett. 38 (2011) L14402. https://doi.org/10.1029/2011GL047911.
63. M.A. Kreslavsky, J.W. Head, D.R. Marchant, Periods of active permafrost layer formation during the geological history of Mars: Implications for circum-polar and mid-latitude surface processes, Planet. Space Sci. 56 (2008) 289–302. https://doi.org/10.1016/j.pss.2006.02.010.
64. W. Dobiński, Permafrost active layer, Earth-Sci. Rev. 208 (2020) 103301. https://doi.org/10.1016/j.earscirev.2020.103301.
65. V. Isaev, A. Kioka, P. Kotov, D.O. Sergeev, A. Uvarova, A. Koshurnikov, O. Komarov, Multi-Parameter Protocol for Geocryological Test Site: A Case Study Applied for the European North of Russia, Energies 15 (2022) 2076. https://doi.org/10.3390/en15062076.
66. V.S. Isaev, A.V. Koshurnikov, A. Pogorelov, R.M. Amangurov, O. Podchasov, D.O. Sergeev, S.N. Buldovich, D.M. Aleksyutina, E.A. Grishakina, A. Kioka, Cliff retreat of permafrost coast in south-west Baydaratskaya Bay, Kara Sea, during 2005-2016, Permafr. Periglac. Process. 30 (2019) 35–47. https://doi.org/10.1002/ppp.1993.
67. H. Jin, Y. Huang, V.F. Bense, Q. Ma, S.S. Marchenko, V. V. Shepelev, Y. Hu, S. Liang, V. V. Spektor, X. Jin, X. Li, X. Li, Permafrost Degradation and Its Hydrogeological Impacts, Water. 14 (2022) 372. https://doi.org/10.3390/w14030372.